



# Geophysical Research Letters

## RESEARCH LETTER

10.1029/2018GL079244

### Key Points:

- Increasing res leads to more tracer uptake, despite shallower mixed layers—highlighting importance of smaller scales in tracer subduction
- Vertical eddy fluxes and diffusive fluxes compensate in interesting ways as the resolution changes
- Increased vertical flux is associated with more energetic submesoscale flows; inertia-gravity waves do not contribute to tracer flux

### Supporting Information:

- Supporting Information S1
- Movie S1
- Movie S2
- Movie S3

### Correspondence to:

D. Balwada,  
db194@nyu.edu

### Citation:

Balwada, D., Smith, K. S., & Abernathey, R. (2018). Submesoscale vertical velocities enhance tracer subduction in an idealized Antarctic Circumpolar Current. *Geophysical Research Letters*, 45. <https://doi.org/10.1029/2018GL079244>

Received 18 JUN 2018

Accepted 10 SEP 2018

Accepted article online 13 SEP 2018

## Submesoscale Vertical Velocities Enhance Tracer Subduction in an Idealized Antarctic Circumpolar Current

Dhruv Balwada<sup>1</sup> , K. Shafer Smith<sup>1</sup> , and Ryan Abernathey<sup>2</sup> 

<sup>1</sup>Courant Institute of Mathematical Sciences, New York University, New York, NY, USA, <sup>2</sup>Lamont-Doherty Earth Observatory, Columbia University, Palisades, NY, USA

**Abstract** Upper-ocean submesoscale fronts, with their associated strong vertical velocities, are often claimed to play a significant role in subducting tracers into the interior. The role of these submesoscale processes in restratifying the mixed layer is now well recognized, but whether they simultaneously flux tracers through the base of the boundary layer remains an open question. We vary the resolution in a semirealistic channel model to control turbulent processes at various scales and study their influence on tracers. It is found that the submesoscale-permitting simulations flux far more tracer downward than the lower-resolution simulations: The 1-km simulation takes up 50% more tracer compared to the 20-km simulation, despite the increased restratifying influence of the resolved submesoscale processes. A full frequency-wave number cross-spectra of the vertical velocity and vertical tracer flux show that the high-frequency inertia-gravity waves that appear in the highest-resolution simulation play no role in irreversible downward tracer transport.

**Plain Language Summary** The oceanic uptake and storage of anthropogenic carbon plays a central role in the global carbon budget, and a significant fraction of this uptake occurs in the Southern Ocean. It is well established that the eddies and fronts, turbulent fluctuations of the flow, are important for this uptake, but the relative influence of different scales is less understood. The eddies and fronts associated with the submesoscale (1–50 km) have been recognized to play a leading role in shallowing the surface boundary layer depths, but the role of the strong vertical velocities, which are generally associated with these features, in transporting fluid below the mixed layer remains unknown. Here we investigate these questions using an idealized Southern Ocean model with an imposed tracer source at the surface. The model resolution is varied as a means to include or omit turbulent processes at various scales. We find that the submesoscale-permitting simulations flux far more tracer downward than the lower-resolution simulations, despite the reduction in the depths of the vigorously mixed boundary layers. We also found that inertia-gravity waves, which are ubiquitous in the ocean and are generally associated with very strong vertical velocities, had no impact on the net tracer flux.

## 1. Introduction

The Earth's oceans store large reservoirs of carbon dioxide, oxygen, and other biogeochemical tracers in the subsurface water column—about 30% of the anthropogenic CO<sub>2</sub> produced in the industrial era has been sequestered in the ocean (Ciais et al., 2014). These tracers are exchanged across the air-sea interface, at a rate controlled in part by the concentration gradient at the boundary between the atmosphere and the ocean. The concentration levels at this interface, for both the atmosphere and ocean, are controlled by the physical processes that connect the interface to the interior of the two reservoirs, in addition to biological or chemical reactions that can locally change the concentrations. The focus of this study is ocean subduction, the process by which material in the boundary layer is physically transported into the interior.

Both mean circulation and transient eddies play an important role in controlling the rate of tracer subduction and setting the mean tracer patterns that are observed in the ocean. Conventionally, the tracers are mixed from the surface to the depth of the mixed layer by strong convection and 3-D mixing in the boundary layers and then transported along isopycnals into the interior of the ocean by mean geostrophic circulations (Stommel, 1979) and mesoscale eddies (Abernathey et al., 2013; Redi, 1982). The Southern Ocean has a particularly strong contribution to net tracer subduction, approximately 40% of the total anthropogenic carbon

was taken south of 40°S (Khaliwala et al., 2009), due to its deep mixed layers, strong overturning circulation, and substantial eddy mixing along the sloping isopycnals that connect the surface to the deep ocean (Sallée et al., 2012).

Estimates from global general circulation models find a significant role for “diffusion” in the subduction of anthropogenic carbon into the ocean’s interior. Bopp et al. (2015), for example, estimate that 65% of the CO<sub>2</sub> absorbed by the ocean is subducted through the base of the mixed layer via diffusive processes. Likewise, Groeskamp et al. (2016) find an important contribution for diffusion in downward transport of carbon. What is called *diffusion* in these studies is in fact the transport modeled by ocean boundary layer mixing schemes and interior mixing schemes, which when tuned, roughly capture the transport due to a wide array of turbulent advective processes, including subduction at fronts that are not currently resolved in coarse climate models. The details and delineation of these processes remain unknown.

Most previous studies of tracer subduction in large domains with realistic forcing have relied on eddy parameterizations to represent mesoscale subgrid-scale transport (Bopp et al., 2015; Gnanadesikan et al., 2015; Karleskind et al., 2011; Lévy et al., 2013). Eddy parameterizations have been developed with the goal of capturing the impact of eddies on the mean stratification, so that a realistic hydrographic solution emerges (Fox-Kemper et al., 2008; Gent & McWilliams, 1990). The component of along isopycnal mixing by eddies, which impacts tracer properties but not stratification, is generally added as a downgradient diffusion (Redi, 1982). Gnanadesikan et al. (2015) showed that the the global ocean uptake of anthropogenic carbon is highly sensitive to the isopycnal diffusion coefficient. This coefficient is generally set to be the same as the Gent-McWilliams coefficient, even though this may not be a good approximation (Abernathey et al., 2013; Smith & Marshall, 2009). Additionally, and probably more relevant for the subduction problem, the way these parameterizations handle the eddy fluxes at the intersection of the well-mixed surface layer and the interior is usually ad hoc (Ferrari et al., 2008).

It is well established at this point that increasing the horizontal resolution in ocean models leads to an increase in the vertical velocities (Capet et al., 2008; Lévy et al., 2001; Lévy et al., 2012; Mahadevan & Archer, 2000; Mahadevan & Tandon, 2006), which is generally attributed to emergence of submesoscale structures and inertia-gravity waves. Strong vertical velocities are generated, for example, by frontogenesis and mixed-layer baroclinic instability. Strain-driven frontogenesis is the formation of sharp buoyancy gradients by mesoscale strain, which results in an associated secondary circulation with strong vertical velocities penetrating to the depth of the front. Mixed-layer baroclinic instability is associated with the release of the available potential energy (APE) stored in the lateral buoyancy gradients in the mixed layer, and the associated vertical velocities peak in the middle of the mixed layer (Callies et al., 2016). While both these mechanisms have been demonstrated to play dominant roles in the restratification of the mixed layers (Fox-Kemper et al., 2008; Su et al., 2018), their contribution to the subduction of tracers has not been fully explored.

It has been hypothesized that strong fronts and submesoscale eddies can be very important in controlling the rate of tracer subduction (Ferrari, 2011; Lévy et al., 2012), and a few idealized numerical experiments have shown support for this notion. Lapeyre and Klein (2006) used a surface quasi-geostrophic model to demonstrate that fronts are a significant contributor to vertical passive tracer flux. Mahadevan and Archer (2000) and Lévy et al. (2001) have pointed that tracer transport due to enhanced fronts and associated vertical velocities can impact the biogeochemical budgets. More recently, Ramachandran et al. (2014), in an idealized submesoscale-permitting primitive equation process model, showed that a coupling between the submesoscale fronts and mesoscale eddies can enhance tracer subduction beyond what would be produced by either alone. Most of these studies have been very idealized; using small domains, where the evolution of the mesoscale field is restricted by the boundaries, and generally in a spin down from an initial condition, usually the spin down of a single front. Thus, it is not completely evident if these results can be generalized to more complex and realistic domains that are in a forced-dissipative equilibrium, which have an unconstrained mesoscale field and surface fronts form and dissipate continuously.

In this study we find that the enhancement of vertical velocities, with increasing resolution, does produce more tracer subduction in a wind- and buoyancy-forced idealized channel simulation, which is meant to be representative of the Southern Ocean. The model and experimental design are described in section 2. The influence of the resolution on the flow itself is explored in section 3. In section 4, we investigate how resolution affects the detailed tracer accumulation budget. In addition, we perform a full frequency-wave number spectral analysis of vertical velocity power and the cross-spectrum of the vertical tracer flux in order to quantify

the relevant temporal and spatial scales that are involved in the subduction process. Importantly, this allows us to isolate the effect of internal waves (which appear in the highest-resolution simulation) from nonwave vertical fluxes. We conclude with a discussion in section 5.

## 2. Model and Experiment Description

A series of numerical experiments, inspired from Abernathey and Cessi (2014), were carried out using the Massachusetts Institute of Technology general circulation model (MITgcm; Marshall, Adcroft, et al., 1997; Marshall, Hill, et al., 1997), in a square channel of size  $2,000 \text{ km} \times 2,000 \text{ km} \times 3 \text{ km}$  on a  $\beta$ -plane centered at approximately  $35^\circ\text{S}$ . The north and south of the domain are blocked by vertical walls, which ensures that no deep overturning circulation can develop. The surface is forced by an atmospheric jet, which causes Ekman pumping to the north and Ekman suction to the south, and a linear temperature restoration, with temperature increasing from south to north. The forcing is held steady, and there is no seasonal or tidal forcing in these simulations. Temperature is the only active tracer contributing to buoyancy, and a linear equation of state was used. The zonal symmetry of the channel and forcing is broken by the presence of a meridional ridge at the bottom that is shaped like a 1-km-high and 150-km-wide Gaussian in the zonal direction and spans the entire meridional extent of the domain.

The numerics of the simulation were set to be the same as those in the LLC4320 simulations (Rocha et al., 2016). The surface boundary layer is parameterized using the K-profile parametrization (KPP; Large et al., 1994), and the numerical viscosity is set by the Modified Leith Viscosity (Fox-Kemper & Menemenlis, 2008). Three horizontal grid spacings are used: 20, 5, and 1 km. The vertical grid is held constant and is the same as that used in the LLC4320, with 76 vertical depth levels, a grid size of 1 m near the surface, increasing to 174 m in the bottom cell. All the results in this paper are from the statistically equilibrated state of the simulations. Further details of the setup, exact forcing functions and numerical parameters are provided in the supporting information.

## 3. Influence of Resolution on the Flow

The physical setup of the experiment—westerly winds and a poleward colder temperature profile—results in an eastward oceanic flow with a large meander setup by the meridional ridge, qualitatively similar to the Antarctic Circumpolar Current (ACC). The isopycnals are strongly sloping and rise to the surface in the south; the forcing acts to steepen them and baroclinic instability, associated with this large APE reservoir, acts to flatten the isopycnals. The baroclinic instability associated with this mean state results in the presence of a highly vigorous eddy field, which is more energetic in the downstream flank of the topography. The presence of the stationary meander and enhanced eddy activity in the downstream flank of the ACC has been identified as key components of the ACC circulation. In addition to being qualitative features of the circulation, they are significant in closing the momentum budget (Thompson & Naveira Garabato, 2014) and strongly contributing to the cross-ACC tracer transport (Thompson & Sallée, 2012). In this study we will investigate the influence that the ridge has on vertical tracer transport by doing comparative analyses in regions upstream and downstream of the ridge. We define two analysis boxes in these regions, shown in Figure 1b.

The turbulence near the surface that would result due to the presence of wind and buoyancy forcing at the interface is parameterized by KPP. This leads to the presence of a mixing layer, where vertical turbulent diffusion is enhanced, and a mixed layer, where the fluid is vertically well mixed and stratification is weak. The depths of these two layers can be different, but for the purpose of this study we focus only on the mixing layer because this is the region where tracer can be vertically transported by enhanced boundary diffusion. The depth of the mixing layer is calculated as the 99th percentile, over the relevant time and horizontal spatial extent, of the depths over which KPP is activated. The deepest mixing layers are seen along the southern boundary, due to cooling at the surface and weak interior stratification that can easily be punctured. The shallowest mixing layers are seen over the ridge, where a strong buoyancy gain is present. Downstream of the ridge, where there is strong eddy activity, the mixing layers are shallower than those upstream of the ridge. This zonal structure presumably results from a combined effect of restratification by baroclinic eddies, destratification by winds, and advection of stratification from the west to east (figures in the supporting information).

In this study we vary the horizontal grid size from 20 to 1 km. To put these scales into context we performed a linear stability analysis on the mean flow and stratification that emerged at different resolutions. In boxes averaged over central regions of the domain, the Rossby deformation wavelength corresponding to the first

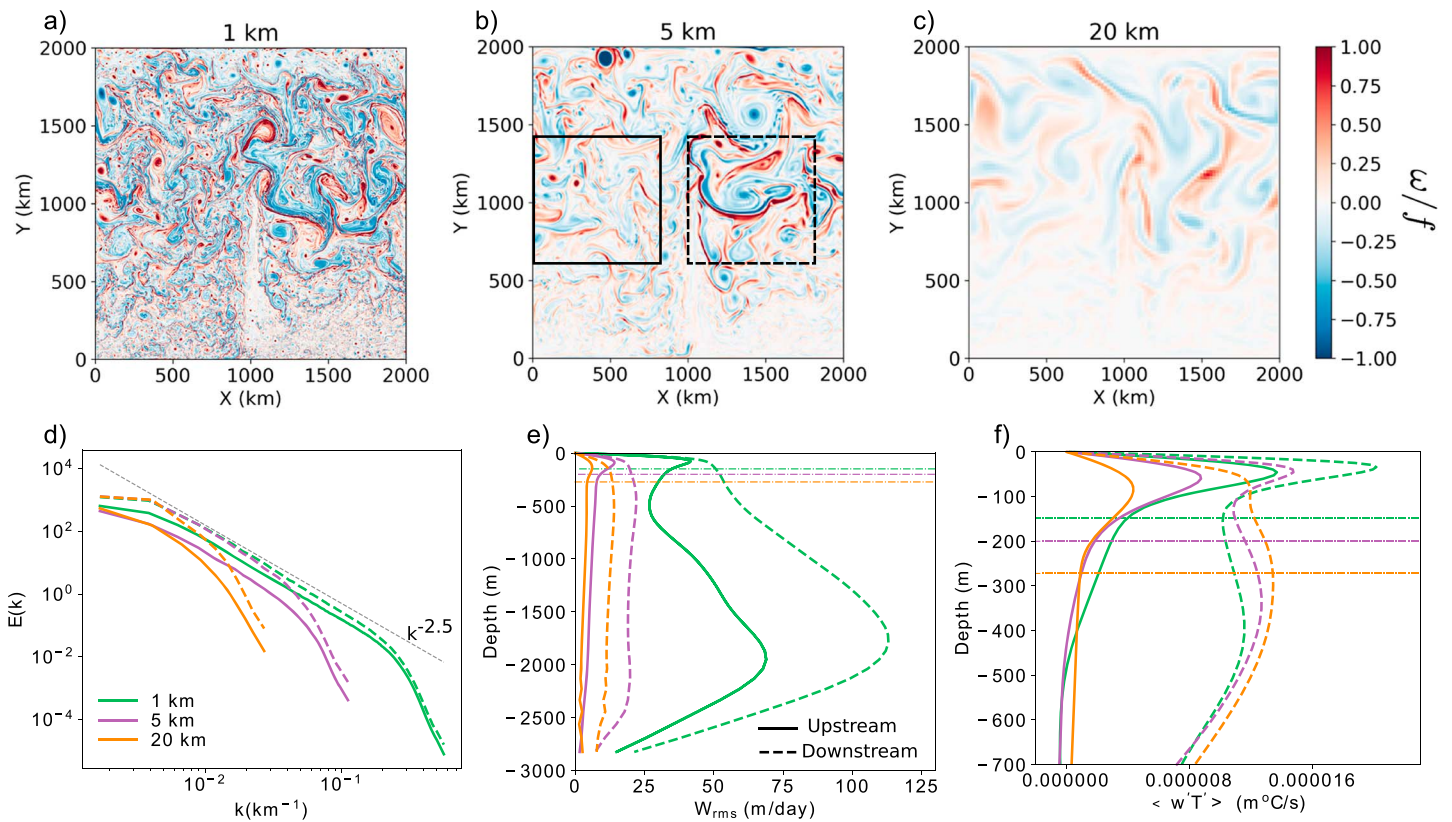


**Figure 1.** Surface vorticity normalized by the Coriolis frequency (Rossby number) for simulations with 1-km (a), 5-km (b), and 20-km (c) simulations. The solid and dashed boxes in (b) represent the regions denoted as the upstream and downstream regions in the analysis. (d) Surface horizontal velocity kinetic energy spectrum for different horizontal resolutions (colors), and for the upstream (solid) and downstream (dashed) regions. A power law of  $k^{-2.5}$ , which visually fits the energy spectrum, is plotted as a thin gray dashed line. (e) The root-mean-square vertical velocity as a function of depth, for different resolutions (colors), and averaged over different regions (dashed/solid). (f) The vertical temperature fluxes as a function of depth for different resolutions (colors) and different regions (dashed/solid). The thin horizontal dash-dot lines represent the KPP mixing layer depths at different resolutions (colors) in (e) and (f).

baroclinic mode is about 150 km, and the fastest growing mode associated with interior baroclinic instability occurs at a similar scale. The so-called mixed-layer deformation scale  $N_{ML} h_{ML} / f$  (McWilliams, 2016) is approximately 1–2 km, and linear stability calculations show a growth peak near to this but at a bit smaller wavelength ( $\sim 500$  m; see the supporting information). These instability scales imply that while interior baroclinic instability is resolved at all resolutions, mixed-layer instability (MLI) is still only marginally permitted in the highest-resolution simulations (generally, the viscous damping extends to length scales that are a factor of 5 greater than the grid scale). Nevertheless, as shown by Uchida et al. (2017), even partial resolution of MLI allows the characteristic influence of this process, restratification and strong vertical velocities, to be present.

Increasing the model resolution leads to the production of more small-scale features—eddies and fronts, as can be seen in the maps of surface vorticity (Figures 1a–1c). The probability density functions of vorticity normalized by the Coriolis frequency ( $f$ ) are positively skewed, with tails extending up to  $8f$  in the 1-km simulation (Figure S7). The isotropic horizontal kinetic energy (KE) spectra at the surface (Figure 1d—see caption for details) shows that the horizontal KE decreases at smaller wavelengths, with a sharp drop in power starting at wavelengths approximately 3 times greater than the smallest allowed wavelength. This sharp dropoff is associated with the numerical viscous dissipation range of the model. The slope of the KE spectrum outside this viscous range is between  $-3$  and  $-2$ , with the spectra being steeper downstream relative to upstream of the ridge. The KE spectra at different resolutions converge outside of the viscous range for the downstream region, while the upstream region in the 1-km simulation shows a marked enhancement in energy at all wavelengths outside of the viscous range. This enhancement may be due to decreased viscous damping of the mesoscale, or it may be associated with an upscale flux of KE originating at the length scales of the MLI, which are permitted in the 1-km simulation. The downstream region does not show a similar effect because either

the MLI scale is not permitted, as the mixing layers are shallower downstream of the ridge, or due to the barotropic governor effect suppressing the growth of shorter wavelength modes (Youngs et al., 2017).

The vertical velocity increases significantly as a function of resolution (Figure 1e), in particular for the 1-km resolution, and is also always greater in the downstream region than in the upstream region. In the upstream region there is a local maximum in vertical velocity in the middle of the mixing layer. This peak is not visible in the downstream region where the vertical velocity associated with deep strong eddies dominates. The vertical velocities in the 5-km resolution are greater than those in the 20-km resolution but have the same vertical structure. However, in the 1-km simulation there is a marked change in the vertical structure, with the appearance of a middepth maximum in vertical velocity around the height of the meridional ridge. Analysis of the vertical velocity in the wave number frequency domain, discussed later, shows that most of the enhancement of the vertical velocity in the 1-km simulation are associated with inertia-gravity waves. By contrast, the increase in vertical velocities from the 20- to 5-km-resolution runs is associated with a more vigorous mesoscale eddy field at subinertial frequencies.

A prominent effect of ocean eddies generated by baroclinic instability, both due to interior baroclinic instability and MLI, is the release of APE by reducing isopycnal slope, thus increasing stratification. Frontogenesis, which is the formation of fronts in the presence of background mesoscale strain, also leads to restratification due to the secondary circulations that develop (McWilliams, 2016). Figure 1f shows that the vertical eddy heat flux as a function of depth for different resolutions and regions is positive or restratifying. All resolutions show a large vertical eddy heat flux in the mixing layer, which increases with resolution. This enhanced vertical eddy heat flux results in restratification of the mixing layer by some combination of MLI and frontogenesis, resulting in a general decrease in mixing layer depths as these processes are better resolved. The downstream region, where the highest eddy kinetic energy (EKE) is observed, shows an interior enhancement of vertical eddy heat flux. This is associated with the interior baroclinic instability and responsible for extracting APE from the large-scale slope of the isopycnals. It is observed that the large-scale structure of the isopycnals is flatter as the resolution is increased (not shown), due to better resolution of the interior baroclinic instability.

#### 4. Influence of Resolution on Tracer Fluxes

The central goal of this work is to study the influence of changing resolution on tracer subduction. To this end we solved the tracer equation,

$$\frac{\partial C}{\partial t} + \mathbf{u} \cdot \nabla C = \nabla \cdot (\kappa \nabla C) + \frac{\partial F_c}{\partial z}, \quad (1)$$

online in the MITgcm, where  $C$  is the tracer concentration,  $t$  is the time,  $\kappa$  is the diffusivity resulting from parameterizations of unresolved processes,  $\mathbf{u}$  is the 3-D velocity field,  $\nabla$  is the gradient operator in 3-D, and  $F_c$  is the tracer forcing.

Here we prescribe  $F_c$  as

$$F_c(z = 0) = k_i[C(z = 0) - C_{\text{atm}}] \quad (2)$$

where  $k_i$  is the transfer velocity and  $C_{\text{atm}}$  is the atmospheric tracer concentration, prescribed as unit value. (Here we choose the arbitrary units to be  $1 \text{ kg/m}^3$ .)  $F_c$  is set to zero below the surface grid point. Thus, our forcing term is in essence a boundary flux forcing and mimics the air-sea exchange flux of a tracer. The piston velocity  $k_i = 2.315 \times 10^{-4} \text{ m/s}$ , which lies in the correct range for transfer velocity of  $\text{CO}_2$  in the Southern Ocean (Garbe et al., 2014). Generally,  $k_i$  is more complex and has a dependence on wind speed, temperature, and other factors, which are ignored for simplicity here. It is assumed that initially, there is no tracer in the domain ( $C(x, y, z, t = 0) = 0$ ). The tracer flux is turned on once the flow field has reached statistical equilibrium and allowed to evolve for 1 year. While this scenario does not represent any specific real world tracer release, it can be thought of as the response of the ocean tracer field to an instantaneous unit change of tracer concentration in the atmosphere, where the atmosphere is assumed to be an infinite source of the tracer. As this is a boundary value problem and the steady state is a trivial one ( $C = C_{\text{atm}}$ ), our study focuses on the time evolution of the solution.

Tracer uptake results from advection and diffusion (primarily a result of the KPP), and the difference in the velocity and diffusivity fields between different resolutions results in qualitatively different tracer clouds (see the supporting information for further discussion of diffusivity in the model). As seen in Figures 2a–2c, at low resolution the tracer penetrates to depth smoothly (uniform brown isosurface), with a few deeper-reaching



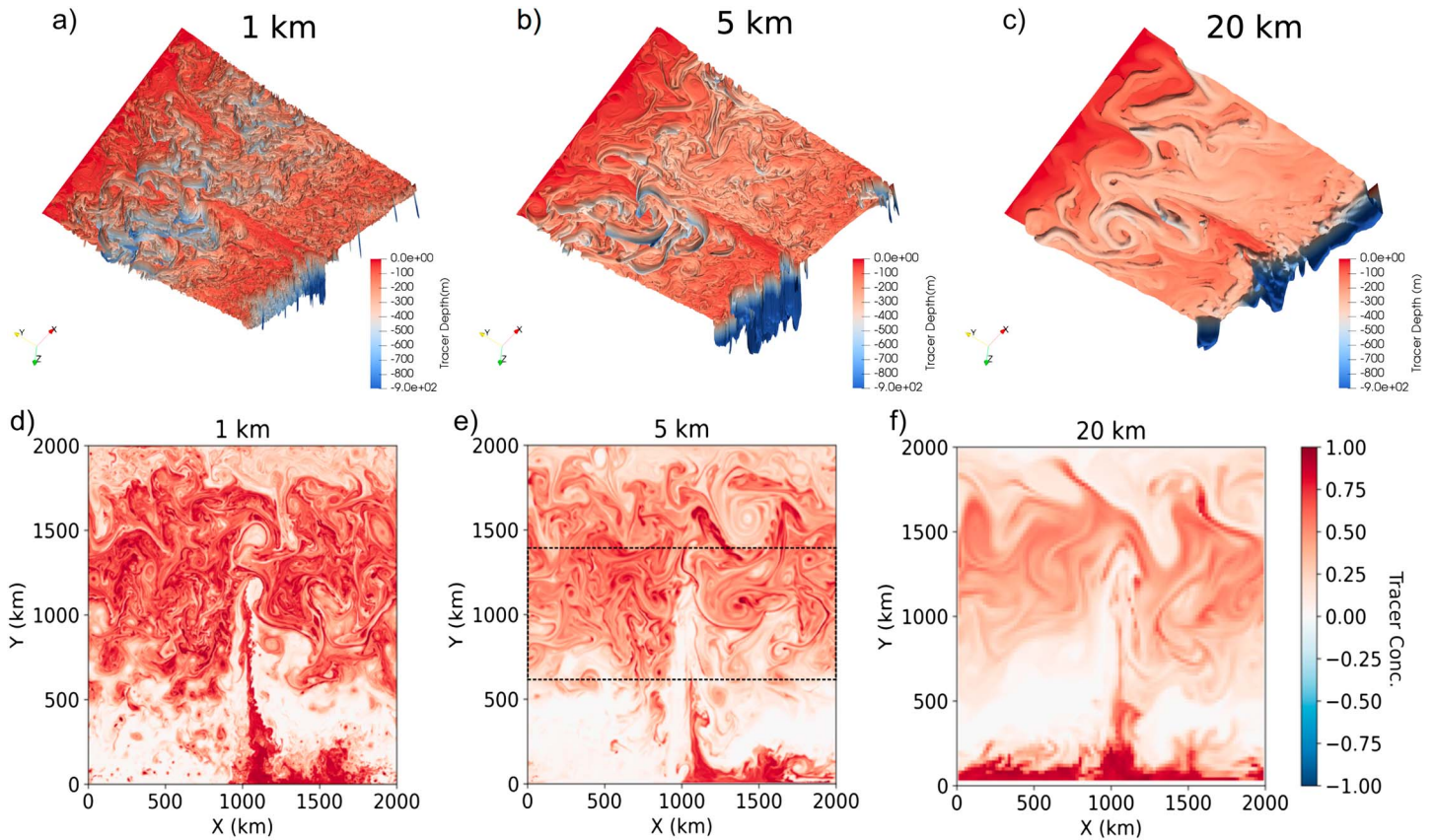


**Figure 2.** Panels (a)–(c) show isosurfaces of tracer concentration 0.1 colored by the surface depth at 30 days after the tracer injection at the surface is started, for resolutions 1, 5, and 20 km, respectively. The view is from a northwest corner at depth, looking toward the surface and southeast. Panels (d)–(f) show tracer concentration fields at a depth of 100 m below the base of the mixing layer and 360 days after the tracer injection for the same three resolutions, respectively. All the tracer analyses in this paper were performed for the region represented by the dashed lines in (e).

filaments associated with the larger fronts and stronger vertical velocities (undulations in the isosurface). At higher resolution, the uniform smooth tracer penetration is curbed (the uniform regions that were brown in the low resolution are now red) due to shallower mixing layers; however, numerous fronts and eddies lead to intermittent penetration of tracer in vertical filaments to significantly greater depths (blue colors). An increase in resolution also causes an increased cascade of tracer variance to smaller scales (Figures 2d–2f), which is correlated to the vorticity structure as seen at the surface. There is a region of deep tracer penetration along the southern boundary, where deep mixing layers are found.

#### 4.1. Tracer Accumulation Budget

We computed a tracer budget in a control volume that is limited meridionally between 600 and 1,400 km (dashed region in Figure 2e), is zonally periodic, and extends vertically from the bottom to depth  $z^*$ . The meridional extent is chosen to minimize the influence of the deep mixing layers along the southern boundary on the budget analysis. Integrating tracer equation (1) over this control volume gives

$$\begin{aligned} \frac{d}{dt} \oint_x \int_{Y_S}^{Y_N} \int_{-H}^{z^*} C \, dx \, dy \, dz \\ = \oint_x \int_{-H}^{z^*} (vC)|_{Y_S} - (vC)|_{Y_N} \, dz \, dx + \oint_x \int_{Y_S}^{Y_N} [-wC + \kappa_v \frac{\partial C}{\partial z} + F_c \delta(z)]|_{z^*} \, dy \, dx \end{aligned} \quad (3)$$

where the left-hand side is the rate of change of the accumulation. The accumulation is defined as the total amount of tracer stored in the control volume, which can increase or decrease by the fluxes at the boundaries of the control volume. The first integral on the right-hand side is the contribution to the increase in accumulation due to horizontal fluxes, and the second integral is the contribution to the increase in accumulation due to the vertical velocity, the vertical diffusion, and the flux of tracer at the surface by the forcing. The function  $\delta(z)$  is the delta function and signifies that the tracer flux is only active at the surface.

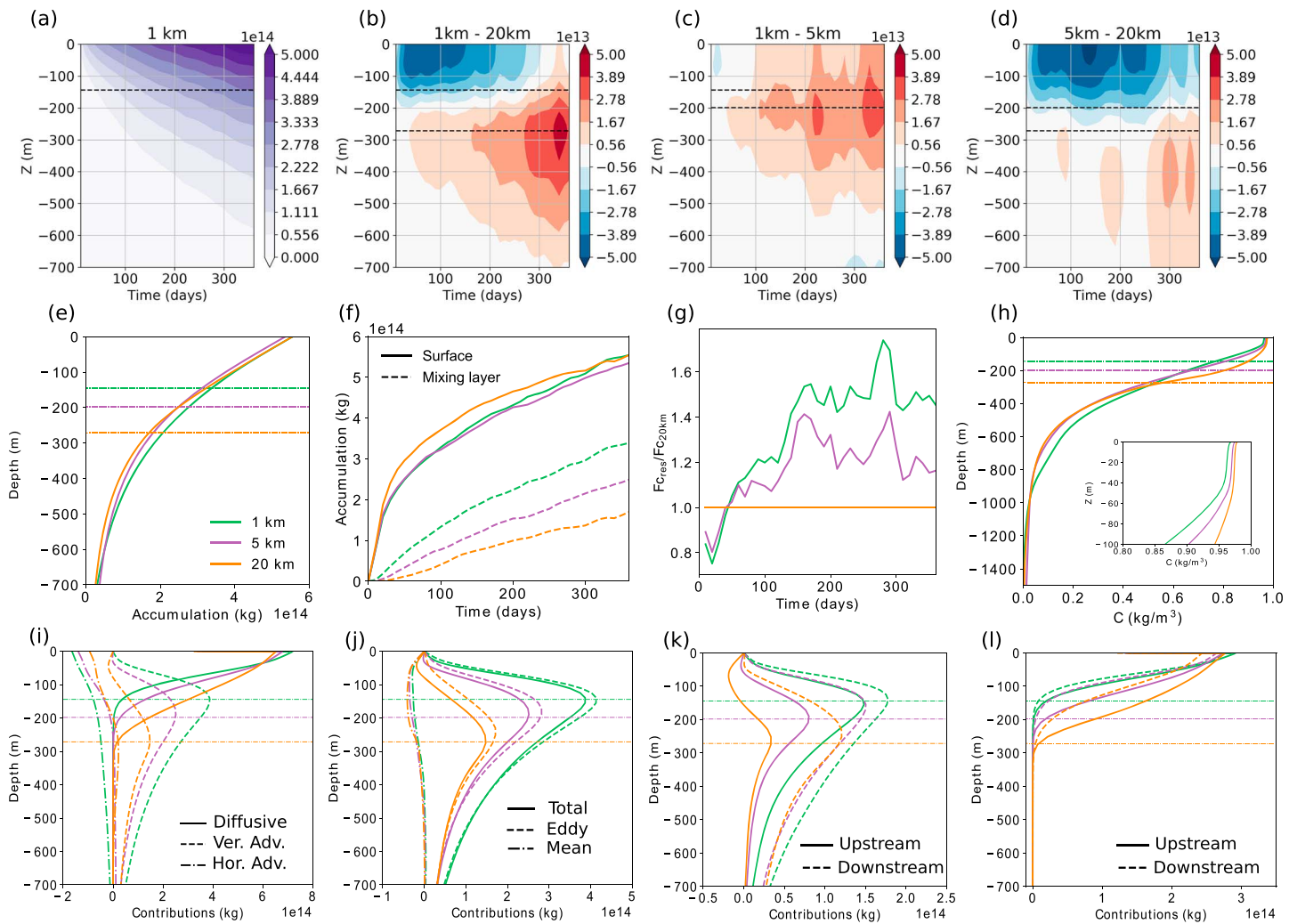


**Figure 3.** (a) Tracer accumulation as a function of time and depth for the the 1-km simulation. The depth of the mixed layer is marked as black dashed line. Panels (b)–(d) show differences in tracer accumulation between the different resolution runs, as marked in the figure titles. The base of the layers for the different resolution simulations are marked in black, with higher resolution having shallower mixed layers. (e) Tracer accumulation as a function of depth for different resolutions (colors) at the end of the 1 year of simulation. The base of the mixed layer is marked as colored horizontal lines. (f) Tracer accumulation as a function of time at the surface (solid) and base of the mixed layer (dashed) for different resolutions (colors). (g) The ratio of the surface tracer forcing for each resolution relative to the surface tracer forcing in the 20-km simulation (colors), averaged over the domain of analysis relative to the tracer forcing. (h) Tracer profiles averaged over the analysis domain as a function of depth for different resolutions (colors) at the end of the 1-year tracer simulation. The thin horizontal lines are the base of the mixed layer in different resolutions. The inset is a zoom into the tracer profiles in the top 100 m. (i) Contributions to the tracer accumulation by different fluxes—horizontal advective (dash-dot), vertical advective (dashed), and vertical diffusive (solid)—as a function of depth and summed over the full year of the tracer simulation for different resolutions (colors). The thin dash-dot horizontal lines are the base of the mixed layers for different resolutions. (j) Decomposition of the total (solid) vertical advective flux into the mean (dash-dot) and eddy (dashed) components summed over the 1 year of the simulation for different resolutions (colors). Panels (k) and (l) show the contributions from the vertical advective and vertical diffusive fluxes summed over the full year and averaged into upstream (solid) and downstream (dashed) regions for different resolutions (colors).

The tracer concentration and tracer accumulation are monotonically decreasing functions of depth and increase in magnitude at all depths as time progresses (Figures 3a, 3h, and S8). Two distinct regimes can be recognized in the evolution of accumulation at the surface (solid lines in Figure 3f). The initial, fast tracer uptake is mediated by the strong vertical diffusion in the mixing layer and leads to a rapid rate of accumulation in the mixing layer for the first couple of months. During this stage, the deeper mixing layers with larger diffusivity of the 20-km run has the largest tracer uptake (seen as negative anomalies extending to the base of the mixing layer in Figures 3b and 3d). The surface flux in the 20-km simulation is the largest during this stage (Figure 3g), as the surface flux (restorative forcing) is controlled by how quickly the tracer is moved away from the surface by the interior vertical advection and diffusion. The relative difference between the 1- and 5-km simulations

during this initial stage is not as dramatic when compared to the 20-km run, showing some potential signs of model convergence in this phase.

Once the mixing layer is partially saturated with tracer, the vertical gradients and the corresponding contribution of vertical diffusion become weaker. At this point the largest tracer variance can be generated at the base of the mixing layer, where the strongest vertical gradients are present (Figure S8). The growth of tracer accumulation below the surface slows down and enters a second phase (Figure 3f, after 80–90 days). In this second phase, the tracer uptake (surface flux) is controlled by the vertical advective flux of tracer through the base of the mixing layer. In this second stage the 1-km simulation has the largest surface flux of tracer (Figure 3g), approximately 50% greater than that of the 20-km simulation.

The temporal sum of different contributions to accumulation over the 1 year of simulation time are shown in Figure 3i. The contribution of the horizontal flux is relatively small and acts to effectively remove tracer from the control volume. The contribution of the vertical diffusive flux is strongest near the surface and decays rapidly at the base of the mixing layer. The magnitude of the vertical diffusive flux reduces with an increase in resolution, as the mixing layer depths and the corresponding diffusivities become smaller. The vertical advective flux shows a maximum near the base of the mixing layer, corresponding to the depth of peak tracer variance (rather than the depth of peak vertical velocity). This contribution increases in magnitude with increased resolution, which is a result of increased vertical velocities with resolution. In this simulation the tracer variance is also primarily generated by the vertical velocities, as the quasi-mean tracer gradients are strongest in the vertical. A decomposition of the vertical advective flux by the a mean and eddy vertical velocity, where the mean is mostly a result of the Ekman-driven vertical velocities, shows that almost all the contributions to the vertical advective flux come from the eddy part (Figure 3j).

Figures 3k and 3l show the relative contributions to the two vertical fluxes in the regions upstream and downstream of the meridional ridge. The vertical advective flux is greater in the region downstream of the ridge, where stronger vertical velocities and deeper fronts are present. The vertical diffusive flux is greater in the upstream region where deeper mixing layers, and correspondingly stronger vertical diffusivities, are present (Figure S11). The contrast between the regions for both the vertical advective and vertical diffusive fluxes is reduced as the resolution is increased.

#### 4.2. Frequency-Wave Number Decomposition of the Flow and Flux

To probe the dominant length and time scales associated with the vertical advective tracer fluxes, we performed spectral decompositions, in wave number and frequency, of the vertical velocities and vertical tracer fluxes. A 2-D wave number decomposition was performed at the horizontal levels of interest and then averaged in the azimuthal wave number direction to project only on the magnitude of the wave number. Hanning windows in both the spatial and temporal axes were imposed to make the data effectively periodic, and power spectra plots are shown in variance-preserving form. More details of the calculation can be found in the supporting information. The combined wave number-frequency decompositions (Figure 4) were performed using hourly model output from day 40 to day 180, counted after the tracer release was started. The wave number versus depth decomposition (Figure 5) was done using 10-day output for the same time period. The time period was chosen to be long enough for the statistics to converge, while also being sufficiently long after the tracer release so that tracer has had time to reach to the deeper depths. This period was also over the time when the peak in the vertical advective tracer flux shows a slow drift in time, as the tracer penetrates deeper, but is slow enough to not significantly influence the wave number-frequency analysis.

The variance-preserving power spectrum of the vertical velocity (Figure 4) shows that below the mixed layer, at a depth of 400 m in the downstream region in the 20- and 5-km runs, the dominant contribution to the vertical velocity is from large wavelengths (100 km) and low frequency (10 days). In the 1-km run, where the vertical velocities were significantly enhanced, the dominant contribution to vertical velocity is from small wavelengths and high frequencies. This dominant contribution at superinertial frequencies is a result of the appearance of internal waves in the 1-km simulation, which can be clearly seen in plots of vertical velocity (note inertia-gravity wave dispersion lines in Figure 4). There is also a region of higher energy that can be seen around wavelength of 5-km and subinertial frequencies, which is most probably related to Doppler shifting of the inertia-gravity waves by the presence of mean flows. The contribution at the larger wavelengths and low frequency, which is present in all simulations, extends toward smaller wavelengths and high frequencies as the resolution is increased. This peak follows a  $\omega \sim k^{3/2}$  turbulent dispersion relationship, which can be



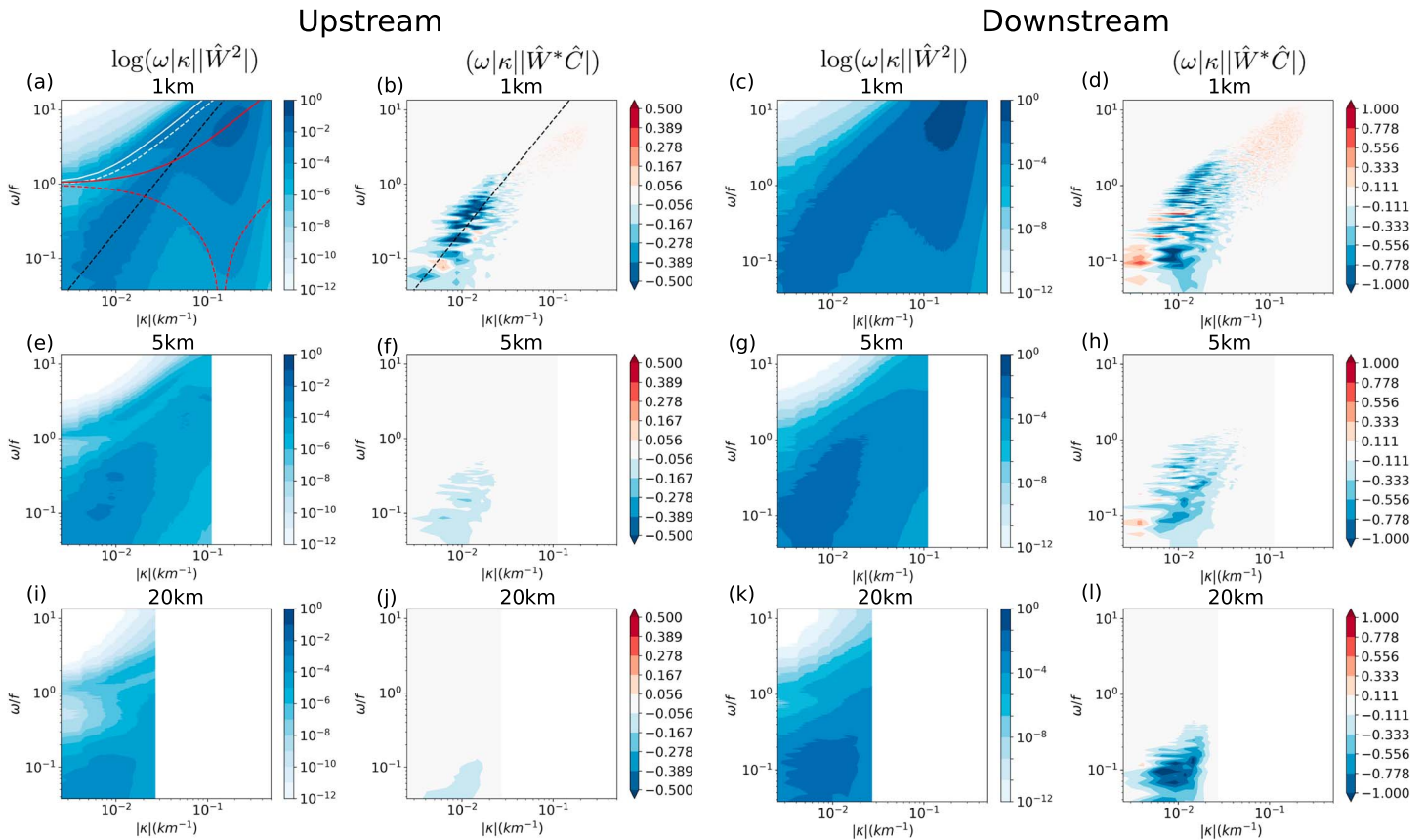


**Figure 4.** Frequency-wave number variance-preserving spectra of vertical velocity and vertical tracer flux at 400 m, averaged over days 40–180 (after tracer release), with inverse wavelength and frequency normalized by the Coriolis frequency as axes. Panels (a), (e), and (i) show the vertical velocity power spectra in the upstream region, and panels (c), (g), and (k) show it in the downstream region. Vertical tracer flux cross-spectra in the upstream region are shown in (b), (f), and (j), and likewise for the downstream region in panels (d), (h), and (l). In (a) and (b) the black dashed line is the turbulent dispersion relationship  $\omega \sim k^{3/2}$  corresponding to a flat vertical KE spectrum. In (a), the white and red lines are the inertia-gravity wave dispersion relationships for the first and fifth normal modes, for the positive (solid) and negative (dashed) branches of the dispersion relationship, in the presence of a mean flow with speed of 3 cm/s.

rationalized by eddy turnover time arguments ( $\omega \sim (k^3 E(k))^{1/2}$ ), and the fact that the vertical KE spectrum has an almost flat spectrum ( $E_w(k) \sim k^0$ ) outside of the dissipation range (not shown).

In contrast to the vertical velocities, the cross-spectrum of the vertical tracer flux at 400 m depth (Figure 4) in all simulations shows a dominant peak at large wavelengths and lower frequencies. Similar to the vertical velocity spectrum, this peak extends to smaller wavelengths and higher frequencies following the turbulent dispersion relationship as the resolution is increased. The magnitude of the cross-spectrum is primarily negative as the vertical tracer flux is pointed downward. A few isolated frequencies and small wave numbers have flux in the upward direction, which would probably disappear with a longer temporal sampling. The dominant peak at superinertial frequencies that is seen in the vertical velocity power spectrum does not have an analogous contribution in the vertical tracer flux cross-spectrum—if anything, the contribution at these wavelengths and frequencies is opposite in sign to the dominant signal. This lack of tracer flux at superinertial frequencies in the 1-km simulation supports the hypothesis that internal waves are inefficient at transporting material.

Figure 5 shows the wave number versus depth dependence of the variance preserving power spectrum of vertical velocity and variance preserving cross-spectrum of vertical tracer flux for the upstream and downstream regions. This analysis is meant to show how the dominant length scales contributing to the tracer transport depend on the depth from the surface. The power spectrum of vertical velocity for the 5- and 20-km runs shows a peak centered at wavelengths slightly larger than 100 km below the mixing layer, which is associated with balanced mesoscale eddies. This peak migrates to smaller wavelengths above the mixing layer and is associated with surface intensified fronts. The variance preserving power spectrum of vertical velocity for the

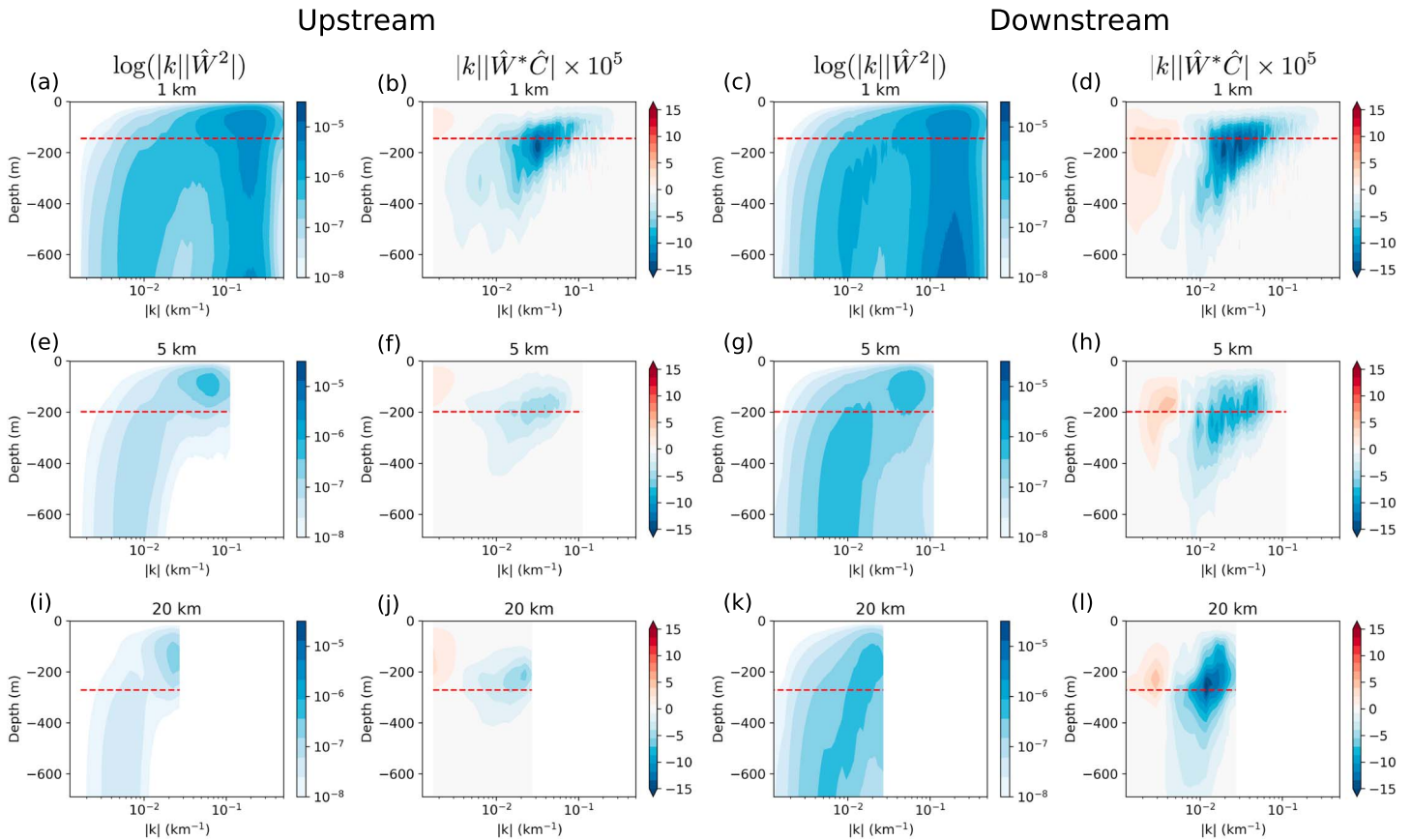


**Figure 5.** Azimuthally and time-averaged (over days 40–180) variance-preserving spectra as a function of inverse wavelength and depth, for vertical velocity in the upstream ((a), (e), and (i)) and downstream ((c), (g), and (k)) regions, and for vertical tracer fluxes in the upstream ((b), (f), and (j)) and downstream ((d), (h), and (l)) regions for different model resolutions. The red horizontal lines represent the base of the mixing layer as each resolution.

1-km run also shows this feature associated with mesoscale eddies at large scales, below the mixed layer, but in addition, the 1-km run also shows a more dominant peak at length scales smaller than 10 km at all depths. This secondary peak, which can be stronger than the mesoscale peak at some depths, is associated with internal waves below the mixing layer. Above the mixing layer, this small-scale peak is presumably a combination of internal waves and surface intensified fronts. The downstream region is more energetic than the upstream region at all resolutions (also seen in Figure 1e). However, the contrast between the two regions is smaller for the 1-km run relative to the lower-resolution runs.

The wave number cross-spectrum of the vertical tracer flux as a function of depth peaks at approximately the depth of the mixing layer, where the vertical tracer flux variance is the highest. In general, the wavelength of the peak in the vertical tracer flux does not change with resolution, but smaller wavelengths make a larger contribution as the resolution is increased. These small-scale fluxes provide a significant contribution to the net tracer flux because the decay in the magnitude of the flux away from the dominant peak along the wave number axis is slow; note that the color scale is not logarithmic (Figure 5). The contribution from the smaller wavelengths is more prevalent closer to the surface, where sharp fronts are clearly seen in the velocity field. However, these small-scale contributions do not completely decay away in the mixing layer, but instead penetrate below the mixing layer and contribute to tracer subduction through the base of the mixing layer. The downstream region has stronger and deeper-reaching vertical tracer fluxes than the upstream region, but this contrast is reduced in the 1-km simulation. This reduction in difference in between the upstream and downstream region tracer fluxes might be related to the greater energization of all length scales that was seen in the horizontal KE spectra in the upstream region (Figure 1).

## 5. Discussion and Conclusions

In this study we tested the hypothesis that the enhanced vertical velocities associated with fronts and sub-mesoscale structures found in our high-resolution simulations should increase net tracer subduction, relative to the low-resolution simulations. The implication is that, in the real ocean, these small-scale features play an important role in the drawdown of tracers from the atmosphere into the deep ocean and might need special attention in eddy parameterizations that are used in coarse-climate simulations. A set of channel simulations forced by winds and buoyancy restoration at the surface, and with a meridional ridge at the bottom, were conducted using the MITgcm. Tracer was forced by continuous restoration of tracer concentration at the surface, after the simulations had equilibrated. We analyzed the nonequilibrium evolution of tracer for 1 year after the tracer forcing was turned on.

Broadly speaking, our experiments are in agreement with the hypothesis: Despite the concomitant increase in mixed-layer stratification, submesoscale motions increase tracer uptake. After an initial phase, during which the mixing layer rapidly saturates with tracer, the tracer flux through the surface is the greatest in the 1-km simulation—about 50% higher than the 20-km simulation. The stronger tracer flux through the surface results from the concentration near the surface being maintained at lower values in the higher-resolution simulations, due to greater flux from the surface into the interior. This enhanced tracer flux to depth is associated with higher vertical velocities in fronts and submesoscale features, which cause tracer to penetrate in curtain like features to depth. At the end of 1 year, the total tracer uptake was highest in the 1-km simulation.

The mixing layer depth, which decreases as resolution is increased, was also found to substantially influence the tracer uptake. The strong diffusivity in the mixing layer caused rapid initial uptake of tracer, with deeper mixing layers taking up more tracer than the shallower mixing layers. This is a result of the KPP imposing a diffusivity that increases with increasing boundary layer depth. A remarkable result is that, while the increase in resolution produces shallower mixed layers with stronger stratification, and hence a smaller tracer uptake in the mixing layer, the net tracer flux due to the combined influence of boundary mixing plus the stronger vertical velocities increased. This indicates that the enhanced vertical velocities more than compensate the reduction in tracer flux due to reduced mixing layer depths. The mixing layer is deeper in the lower-resolution simulations, but it is also more isolated from the interior.

Our simulations have a meridional ridge that produces a region of enhanced variability on its downstream side. These downstream regions have previously been identified as hot spots of lateral stirring (Naveira Garabato et al., 2011; Thompson & Sallée, 2012). Our study shows that this downstream region also has stronger and deeper-reaching fronts, which are responsible for a large vertical tracer flux in this region. However, this dichotomy between the upstream versus downstream vertical tracer flux is reduced in the highest-resolution simulation. This might be a result of the enhanced submesoscale activity that is seen in the upstream region of the 1-km simulation, as the MLI scale is resolved. Additionally, this upstream region in the 1-km simulation has greater energy at the larger scales relative to the lower-resolution simulations, presumably due to an inverse energy cascade acting upscale from the submesoscale, which may produce more energetic and larger eddies with deeper reaching vertical velocities.

A spectral decomposition of the vertical velocity and vertical tracer flux revealed that smaller-scale features are involved in tracer fluxes at shallower depths, but the larger-scale features also contribute substantially. At deeper depths, where smaller-scale features have decayed, the tracer flux is maintained by the larger-scale vertical motions. The smaller-scale features do not decay completely at the base of the mixing layer, but instead penetrate below it, and are significant contributors to the tracer subduction into the interior. There was also a significant enhancement in vertical velocity in the 1-km simulation at small scales associated with inertia-gravity waves that spontaneously emerged at this resolution. However, these internal waves had no influence on the vertical tracer flux.

Even at 1-km resolution, we have no expectation that our simulations are converged with respect to resolution, and they clearly do not even fully resolve MLI or other frontogenetic processes that characterize the ocean's submesoscales. Nevertheless, our results strongly suggest that small-scale transport can play a leading-order role in the vertical transport of tracers in the Southern Ocean and likely elsewhere.

In future work, it would be beneficial to address whether the enhanced transport through the base of the mixed layer could be attributed to strong vertical velocities generated by MLI, strain driven frontogenesis, some combination of both, or interaction of these processes with the mesoscales. Current MLI

parameterizations do not enhance transport through the base of the mixed layer and might be missing an important contribution to subduction. Further, it is also important to address the influence of seasonality on these transport mechanisms, as the submesoscale activity in the ocean shows a clear seasonal waxing and waning cycle. Finally, quantifying the contribution of this transport pathway to the uptake of anthropogenic carbon and the upwelling of nutrients such as iron is of paramount importance.

## Acknowledgments

We would like to thank Takaya Uchida, Roy Barkan, and Baylor Fox-Kemper for helpful discussions. We are grateful for support from NASA award NNX16AJ35G. We also thank NYU, the NYU Abu Dhabi Institute, and Columbia University for the use of high-performance computing facilities. The Columbia University's Shared Research Computing Facility project is supported by NIH Research Facility Improvement grant 1G20RR030893-01 and associated funds from the New York State Empire State Development, Division of Science Technology and Innovation (NYSTAR) contract C090171, both awarded 15 April 2010. Scripts used in this analysis and for generating figures in this manuscript can be obtained on the author's github ([github.com/dhrubwalwada/submesoscale\\_subduction\\_GRL](https://github.com/dhrubwalwada/submesoscale_subduction_GRL)).

## References

- Abernathy, R., & Cessi, P. (2014). Topographic enhancement of eddy efficiency in baroclinic equilibration. *Journal of Physical Oceanography*, 44(8), 2107–2126.
- Abernathy, R., Ferreira, D., & Klocker, A. (2013). Diagnostics of isopycnal mixing in a circumpolar channel. *Ocean Modelling*, 72, 1–16.
- Bopp, L., Lévy, M., Resplandy, L., & Sallée, J.-B. (2015). Pathways of anthropogenic carbon subduction in the global ocean. *Geophysical Research Letters*, 42, 6416–6423. <https://doi.org/10.1002/2015GL065073>
- Callies, J., Flierl, G., Ferrari, R., & Fox-Kemper, B. (2016). The role of mixed-layer instabilities in submesoscale turbulence. *Journal of Fluid Mechanics*, 788, 5–41.
- Capet, X., McWilliams, J. C., Molemaker, M. J., & Shchepetkin, A. (2008). Mesoscale to submesoscale transition in the California Current system. Part I: Flow structure, eddy flux, and observational tests. *Journal of physical oceanography*, 38(1), 29–43.
- Ciais, P., Sabine, C., Bala, G., Bopp, L., Brovkin, V., Canadell, J., et al. (2014). Carbon and other biogeochemical cycles. In O. Edenhofer, et al. (Eds.), *Climate change 2013: The physical science basis. Contribution of Working Group I to the Fifth Assessment Report of the Intergovernmental Panel on Climate Change* (pp. 465–570). United Kingdom and New York, NY, USA: Cambridge University Press.
- Ferrari, R. (2011). A frontal challenge for climate models. *Science*, 332(6027), 316–317.
- Ferrari, R., McWilliams, J. C., Canuto, V. M., & Dubovikov, M. (2008). Parameterization of eddy fluxes near oceanic boundaries. *Journal of Climate*, 21(12), 2770–2789.
- Fox-Kemper, B., Ferrari, R., & Hallberg, R. (2008). Parameterization of mixed layer eddies. Part I: Theory and diagnosis. *Journal of Physical Oceanography*, 38(6), 1145–1165.
- Fox-Kemper, B., & Menemenlis, D. (2008). Can large eddy simulation techniques improve mesoscale rich ocean models? *Ocean modeling in an eddying regime*, 177, 319–337.
- Garbe, C. S., Rutgersson, A., Boutin, J., De Leeuw, G., Delille, B., Fairall, C. W., et al. (2014). Transfer across the air-sea interface. In P. Liss & M. Johnson (Eds.), *Ocean-Atmosphere interactions of gases and particles* (pp. 55–112). Berlin, Heidelberg: Springer.
- Gent, P. R., & McWilliams, J. C. (1990). Isopycnal mixing in ocean circulation models. *Journal of Physical Oceanography*, 20(1), 150–155.
- Gnanadesikan, A., Pradal, M.-A., & Abernathy, R. (2015). Isopycnal mixing by mesoscale eddies significantly impacts oceanic anthropogenic carbon uptake. *Geophysical Research Letters*, 42, 4249–4255. <https://doi.org/10.1002/2015GL064100>
- Groeskamp, S., Lenton, A. A., Matear, R. J., Sloyan, B., & Langlais, C. (2016). Anthropogenic carbon in the ocean-surface to interior connections. *Global Biogeochemical Cycles*, 30, 1682–1698. <https://doi.org/10.1002/2016GB005476>
- Karleskind, P., Lévy, M., & Mémery, L. (2011). Subduction of carbon, nitrogen, and oxygen in the northeast Atlantic. *Journal of Geophysical Research*, 116, C02025. <https://doi.org/10.1029/2010JC006446>
- Khatiwal, S., Primeau, F., & Hall, T. (2009). Reconstruction of the history of anthropogenic CO<sub>2</sub> concentrations in the ocean. *Nature*, 462(7271), 346.
- Lapeyre, G., & Klein, P. (2006). Impact of the small-scale elongated filaments on the oceanic vertical pump. *Journal of Marine Research*, 64(6), 835–851.
- Large, W. G., McWilliams, J. C., & Doney, S. C. (1994). Oceanic vertical mixing: A review and a model with a nonlocal boundary layer parameterization. *Reviews of Geophysics*, 32(4), 363–403.
- Lévy, M., Bopp, L., Karleskind, P., Resplandy, L., Éthé, C., & Pinsard, F. (2013). Physical pathways for carbon transfers between the surface mixed layer and the ocean interior. *Global Biogeochemical Cycles*, 27, 1001–1012. <https://doi.org/10.1002/gbc.20092>
- Lévy, M., Ferrari, R., Franks, P. J., Martin, A. P., & Rivière, P. (2012). Bringing physics to life at the submesoscale. *Geophysical Research Letters*, 39, L14602. <https://doi.org/10.1029/2012GL052756>
- Lévy, M., Klein, P., & Treguer, A.-M. (2001). Impact of sub-mesoscale physics on production and subduction of phytoplankton in an oligotrophic regime. *Journal of Marine Research*, 59(4), 535–565.
- Mahadevan, A., & Archer, D. (2000). Modeling the impact of fronts and mesoscale circulation on the nutrient supply and biogeochemistry of the upper ocean. *Journal of Geophysical Research*, 105(C1), 1209–1225.
- Mahadevan, A., & Tandon, A. (2006). An analysis of mechanisms for submesoscale vertical motion at ocean fronts. *Ocean Modelling*, 14(3–4), 241–256.
- Marshall, J., Adcroft, A., Hill, C., Perelman, L., & Heisey, C. (1997). A finite-volume, incompressible Navier Stokes model for studies of the ocean on parallel computers. *Journal of Geophysical Research*, 102(C3), 5753–5766.
- Marshall, J., Hill, C., Perelman, L., & Adcroft, A. (1997). Hydrostatic, quasi-hydrostatic, and nonhydrostatic ocean modeling. *Journal of Geophysical Research*, 102(C3), 5733–5752.
- McWilliams, J. C. (2016). Submesoscale currents in the ocean. *Proceedings of the Royal Society A*, 472(2189) 20160117.
- Naveira Garabato, A. C., Ferrari, R., & Polzin, K. L. (2011). Eddy stirring in the Southern Ocean. *Journal of Geophysical Research*, 116, C09019. <https://doi.org/10.1029/2010JC006818>
- Ramachandran, S., Tandon, A., & Mahadevan, A. (2014). Enhancement in vertical fluxes at a front by mesoscale-submesoscale coupling. *Journal of Geophysical Research: Oceans*, 119, 8495–8511. <https://doi.org/10.1002/2014JC010211>
- Redi, M. H. (1982). Oceanic isopycnal mixing by coordinate rotation. *Journal of Physical Oceanography*, 12(10), 1154–1158.
- Rocha, C. B., Gille, S. T., Chereskin, T. K., & Menemenlis, D. (2016). Seasonality of submesoscale dynamics in the Kuroshio Extension. *Geophysical Research Letters*, 43, 11,304–11,311. <https://doi.org/10.1002/2016GL071349>
- Sallée, J.-B., Matear, R. J., Rintoul, S. R., & Lenton, A. (2012). Localized subduction of anthropogenic carbon dioxide in the Southern Hemisphere oceans. *Nature Geoscience*, 5(8), 579–584.
- Smith, K. S., & Marshall, J. (2009). Evidence for enhanced eddy mixing at middepth in the Southern Ocean. *Journal of Physical Oceanography*, 39(1), 50–69.
- Stommel, H. (1979). Determination of water mass properties of water pumped down from the Ekman layer to the geostrophic flow below. *Proceedings of the National Academy of Sciences*, 76(7), 3051–3055.
- Su, Z., Wang, J., Klein, P., Thompson, A. F., & Menemenlis, D. (2018). Ocean submesoscales as a key component of the global heat budget. *Nature Communications*, 9(1), 775.



- Thompson, A. F., & Naveira Garabato, A. C. (2014). Equilibration of the antarctic circumpolar current by standing meanders. *Journal of Physical Oceanography*, 44(7), 1811–1828.
- Thompson, A. F., & Sallée, J.-B. (2012). Jets and topography: Jet transitions and the impact on transport in the Antarctic Circumpolar Current. *Journal of physical Oceanography*, 42(6), 956–972.
- Uchida, T., Abernathey, R., & Smith, S. (2017). Seasonality of eddy kinetic energy in an eddy permitting global climate model. *Ocean Modelling*, 118, 41–58.
- Youngs, M. K., Thompson, A. F., Lazar, A., & Richards, K. J. (2017). ACC, meanders, energy transfer, and mixed barotropic-baroclinic instability. *Journal of Physical Oceanography*, 47(6), 1291–1305.